2016

Tuning Complexity by Lithiation: A Family of Intergrowth Structures Using Condensed hypho-Icosahedra in the Li-Doped Ca–Zn System

Qisheng Lin
The Ames Laboratory, qslin@ameslab.gov

Ran Zhu
Iowa State University

Gordon J. Miller
Iowa State University, gmiller@iastate.edu

Inorganic Chemistry

Article

pubs.acs.org/IC

Tuning Complexity by Lithiation: A Family of Intergrowth Structures Using Condensed *hypho*-Icosahedra in the Li-Doped Ca−Zn System

Qisheng Lin,*[,†] Ran Zhu,[‡] and Gordon J. Miller[†,‡]

[†]Division of Materials Science and Engineering, Ames Laboratory, U.S. Department of Energy, Ames, Iowa 50011, United States

[‡]Department of Chemistry, Iowa State University, Ames, Iowa 50011, United States

Supporting Information

ABSTRACT: Cluster chemistry of intermetallics with valence electron counts (VECs) in the range of 2.0−3.0 is intriguing. Lithiation of polar intermetallics in this VEC region is found to be an effective chemical route to produce new complex structures with different stability mechanisms. In this work, two new complex intermetallic structures have been discovered in the Ca−Li−Zn system: $Ca_{12}Li_xZn_{59-x}$ and $Ca_{15}Li_xZn_{75-x}$. $Ca_{12}Li_xZn_{59-x}$, $x \approx 5.65(3)-14.95(3)$, forms in the trigonal space group $R\bar{3}m$, with $a = 9.074(1)-9.1699(2)$ Å, $c = 53.353(1)-53.602(1)$ Å, and $Z = 3$. In comparison, $Ca_{15}Li_xZn_{75-x}$, $x \approx 19.07(2)$, crystallizes in the space group $P6_3/mmc$, with $a \approx 9.183(1)$ Å, $c \approx 45.191(5)$ Å), and $Z = 2$. Both structures are members of a large intergrowth family featuring slabs of dimers (D) and trimers (T) stacking along [001], with the sequences DTDDTDDTD for $Ca_{12}Li_xZn_{59-x}$ and TDDDTDDD for $Ca_{15}Li_xZn_{75-x}$. Each dimer consists of two face-sharing Zn-centered *hypho*-icosahedra, and each trimer comprises a Li-centered icosahedron sandwiched by two *hypho*-icosahedra. This intergrowth family includes several known intermetallic structure types involving very electropositive metals, e.g., $SrMg_{5.2}$, $Ba_2Li_{4.21}Al_{4.79}$, and $Sr_9Li_{17.5}Al_{25.5}$. Because of cluster defects and condensation, both $Ca_{12}Li_xZn_{59-x}$ and $Ca_{15}Li_xZn_{75-x}$ are electronically akin to close-packed metals, and their structural stabilities can be interpreted by a Hume-Rothery mechanism rather than the Zintl−Klemm concept.

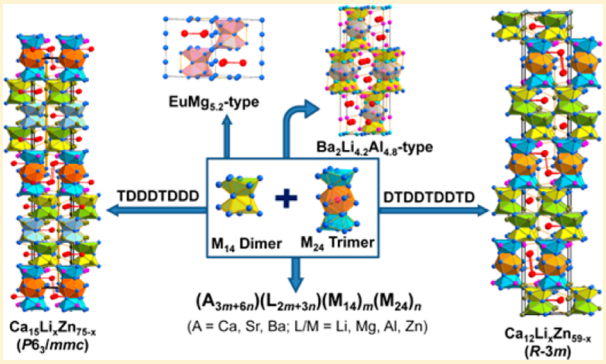

INTRODUCTION

Zn-rich intermetallics exhibit various interesting structural motifs and bonding patterns. In general, they show characteristics of metals, similar to the dominant component Zn, which means that traditional electron counting schemes could be disfavored due to electron delocalization. For example, the Zintl−Klemm concept rationalizes very well the double-diamond, NaTl-type structures of LiAl, LiGa, and LiIn at ambient conditions,[1] but LiZn of the same type is an exception because only three instead of four electrons can be assigned to Zn.[2] On the other end, the structural stability of some Zn-rich phases, e.g., γ-brass-type Cu_5Zn_8,[3] is dominated by Fermi surface−Brillouin zone interactions,[4] as manifested by the Hume-Rothery concept.[5,6] In other words, depending on the composition and structure, Zn-rich intermetallics can follow different composition−structure stabilization mechanisms. However, no single formalism can clearly tell how a Zn-rich intermetallic structure is stabilized, in contrast to classical Zintl phases, which are dominated by group 13 or 14 elements.

Recently, lithiation of binary $CaZn_2$ has proved to be able to transform a three-dimensional (3D) framework of tetrahedrally coordinated Zn into complex structures of $Ca_{\sim 30}Li_{3+x}Zn_{60-x}$ ($x = 0.44-1.38$) containing an extended network of Zn_3 triangles, Zn_{12} icosahedra, and $(Li,Zn)_{18}$ tubular clusters.[7] The presence of just ∼4 mol % Li results in a significant structural change, demonstrating an important role of valence electron counts (VECs) per Zn atom on the structural stability of Zn-rich intermetallics. That is, as the VEC/Zn decreases, more condensed and more complex polyhedra form. In fact, the same trend is also observed for Ca−Zn binaries. For example, the structure of $CaZn_3$ features chains of face-sharing icosahedra bridged by Zn-atom spacers,[8] in contrast to the diamond-like framework of Zn in $CaZn_2$.[9] $CaZn_5$ exhibits hexagonal tunnels defined by corner-sharing trigonal-bipyramidal Zn_5 clusters,[10] $CaZn_{11}$ is formed by corner-sharing hexagonal antiprisms of Zn,[11] and the Zn framework in $CaZn_{13}$[12] is formed by interconnected icosahedra, resulting in snub cubes centered by Ca. The VEC/Zn values of $CaZn_x$ (x = 2, 3, 5, 11, and 13) monotonically decrease from 3.00 to 2.67, to 2.40, to 2.18, and finally to 2.15. Remarkably, the structure change arising from decreasing VEC by lithiation does not simply repeat these structures seen for binaries but results in new types of clusters, e.g., $Ca_{\sim 30}Li_{3+x}Zn_{60-x}$.[7] This suggests lithiation of binaries to be a useful practical route to produce new intermetallics with low VEC. As a further test to see how the structure and clusters evolve as a function of VEC, this work focuses on lithiation reactions stemming from $CaZn_5$.

Received: March 11, 2016
Published: April 26, 2016

DOI: 10.1021/acs.inorgchem.6b00612
Inorg. Chem. 2016, 55, 5041−5050

These results could lend some useful clues to rationalize the structure stability for VEC/Zn values between 2.0 and 3.0.

Herein, the synthesis, structure, and some thoughts about valence electron counting for two unprecedented structures with compositions close to $Ca(Li,Zn)_{\sim 5}$ are reported. These two new compounds represent two members of a potentially larger family of intergrowth structures containing dimers of two face-sharing *hypho*-icosahedra (a *hypho*-icosahedron is an icosahedron with three missing vertices) and trimers of two *hypho*-icosahedra sandwiching an icosahedron by sharing faces. In contrast to the Zintl-like $Ca_{\sim 30}Li_{3+x}Zn_{60-x}$,[7] the present two structures have lower VEC or e/a values, and electronic structure analyses confirm a Fermi surface−Brillouin zone interaction as their structural stabilization mechanism. This work nicely illustrates lithiation as an applicable route to achieve novel intermetallics demanded by Zintl−Klemm concepts or Hume-Rothery mechanisms.

EXPERIMENTAL SECTION

Synthesis. All reactants (Alfa Aesar; as-received Zn shot, 99.99%; dendritic Ca pieces, 99.95%; Li ingot, 99.9%) were weighed in an Ar-filled glovebox (≤0.1 ppm of H_2O by volume). Ca and Li were used after surface cleaning by scalpel blades. Mixtures of metals (∼400 mg in total weight) were placed in Ta tubes (⌀ ≈ 9.5 mm), which were subsequently sealed using an arc welder and enclosed in a silica jacket ($<10^{-6}$ Torr). The following heating profile was applied for all reactions unless otherwise specified: heated to 700 °C at a rate of 120 °C/h, held there for 2 h, cooled to 400 °C at a rate of 5 °C/h, annealed there for 1 week, and then quenched in cold water.

Both the $Ca_{12}Li_xZn_{59-x}$ and $Ca_{15}Li_xZn_{60-x}$ phases are brittle and have metallic luster. The metallic luster of $Ca_{12}Li_xZn_{59-x}$ remains after exposure to air at room temperature for several weeks. In contrast, $Ca_{15}Li_xZn_{60-x}$ crystals change to gray over 1 week, presumably because of the larger Li content.

Powder X-ray Diffraction. Powder X-ray diffraction measurements were performed at room temperature using a STOE Stadi P powder X-ray diffractometer equipped with an image plate and Cu Kα_1 radiation (λ = 1.5406 Å). Each powder sample was dispersed between two acetate films with the aid of a small amount of grease. Because of possible peak shifts arising from factors such as variable sample thickness, amount of grease used, and possible uneven surface of the acetate film, a small amount (∼10% by volume) of polycrystalline Si standard (NIST 640b) was added to each powder sample so that the lattice parameters can be consistently calibrated.

Structural Analyses. Single-crystal X-ray diffraction data were collected at room temperature (293 K) using a Bruker SMART APEX II diffractometer (Mo Kα radiation; λ = 0.71073 Å). Mixed ω and φ scan modes were used for data collection over a 2θ range of ∼3−60°, with the duration of exposure set at 10−20 s/frame. Data reduction, integration, unit cell refinements, and absorption corrections were accomplished with the aid of the *APEX2* program.[13] Initial structural models were obtained by direct methods. Full-matrix least-squares refinements on F^2 and difference Fourier analyses of these models were carried out using *SHELXTL 6.1*.[14]

Direct methods successfully solved both structures. Assignments of the Ca and Zn atom sites were based on the environments and interatomic distances, and Li assignments were obtained by difference Fourier maps. Zn/Li mixings were suggested by isotropic displacement parameters and confirmed by experimental compositions and further structural refinements. No Ca/Li mixing was suggested in either structure. A total of five crystals were structurally refined for $Ca_{12}Li_xZn_{59-x}$ (three from different loadings and two from the same loading) and one for $Ca_{15}Li_xZn_{60-x}$. Therefore, structures of $Ca_{12}Li_{14.95(3)}Zn_{44.05(3)}$ and $Ca_{15}Li_{19.07(2)}Zn_{55.93(2)}$ with similar compositions are given as examples in the following discussion. Details of data collection and structural refinements for $Ca_{12}Li_{14.95(3)}Zn_{44.05(3)}$ and $Ca_{15}Li_{19.07(2)}Zn_{55.93(2)}$ are summarized in Table 1. Atomic positions and equivalent isotropic displacement parameters for $Ca_{12}Li_{14.95(3)}Zn_{44.05(3)}$ and $Ca_{15}Li_{19.07(2)}Zn_{55.93(2)}$ are listed, respectively, in Tables 2 and 3. Further crystallographic information in the form of a CIF file is available in the Supporting Information.

Table 1. Crystal Data and Structural Refinements for $Ca_{12}Li_{14.95(3)}Zn_{44.05(3)}$ and $Ca_{15}Li_{19.07(2)}Zn_{55.93(2)}$

formula	$Ca_{12}Li_{14.95(3)}Zn_{44.05(3)}$	$Ca_{15}Li_{19.07(2)}Zn_{55.93(2)}$
fw	3464.46	4389.40
space group, Z	$R\bar{3}m$, 3	$P6_3/mmc$, 2
a (Å)	9.1699(2)	9.183(1)
c (Å)	53.602(1)	45.191(5)
vol (Å^3)	3903.4(2)	3300.4(9)
d_{calcd} (g/cm^3)	4.421	4.417
abs coeff (mm^{-1})	21.033	21.034
reflns coll./R_{int}	19507/0.0922	24214/0.1229
data/restraints/param	1249/0/88	1307/0/110
GOF on F^2	1.020	1.026
R1/wR2 [$I > 2\sigma(I)$]	0.0293/0.0445	0.0376/0.0710
R1/wR2 (all data)	0.0562/0.0505	0.0886/0.0860
peak/hole (e/Å^3)	1.905/−1.199	1.788/−1.261

Electronic Structure Calculations. Tight-binding calculations were performed self-consistently by the linear muffin-tin orbital (LMTO) method within the atomic sphere approximation (ASA) using the Stuttgart code.[15−17] Scalar relativistic corrections were included. The radii of the Wigner−Seitz (WS) spheres were assigned automatically so that the overlapping potentials would be the best possible approximations to the full potentials. The WS radii (Ca, ≈1.85−1.95 Å; Li, ≈1.30−1.50 Å; Zn, ≈1.40−1.57 Å) were automatically scaled by the program to achieve interatomic overlaps no larger than 16% with no additional empty spheres. The basis sets of Ca 4s3d(4p), Li 2s(2p), and Zn 4s4p wave functions were employed, with downfolded functions in parentheses. Zn 3d orbitals were treated as filled core functions.

Electronic structure calculations for the trigonal-phase $Ca_{12}Li_{14.95(3)}Zn_{44.05(3)}$ were carried out using two hypothetical models: (I) "$Ca_{12}LiZn_{58}$" assumes Li atoms occupying the centers of icosahedra only (Li15), with all other formally anionic sites being occupied by Zn; (II) "$Ca_{12}Li_{15}Zn_{44}$" assumes Li occupying Li4, Zn/Li5, Zn/Li12, and Li15 sites (all Li-dominated sites at this composition), so that the composition of this model is close to that refined by single-crystal diffraction analyses. Both models yielded essentially similar results except that the bandwidth for the Li-poor "$Ca_{12}LiZn_{58}$" model is wide with fewer Li 2s states below the Fermi energy (E_F); see Figure S1 in the Supporting Information. Crystal orbital Hamilton population (COHP)[18] analyses for selected atom pairs were also conducted. From these COHP results, the contribution of the covalent part of a particular interaction to the total bonding energy of the crystal can be evaluated. The weighted integration of −COHP up to E_F (−ICOHP) is an indicator of relative bond strengths. Reciprocal space integrations for both models were performed based on a 24 × 24 × 24 mesh of 1313 k points in the irreducible wedges of the Brillouin zone. For the hexagonal-phase $Ca_{15}Li_{19.07(2)}Zn_{55.93(2)}$, calculations were made on the model "$Ca_{15}Li_{18}Zn_{57}$", in which all Li-dominanted sites are occupied by Li. Integrations for this model were performed over a 36 × 36 × 12 mesh of 889 k points in the irreducible wedge of the Brillouin zone.

RESULTS AND DISCUSSION

Syntheses and Phase Widths. The $Ca_{12}Li_xZn_{59-x}$ phase was first obtained as a minor product in a study of the $(Ca_{1-x}Li_x)ZnSi$ system, and its composition and structure were established as $Ca_{12}Li_{9.44(3)}Zn_{49.56(3)}$ [$R\bar{3}m$, Z = 3, a = 9.110(1) Å, and c = 53.345(7) Å] according to single-crystal X-ray diffraction analyses. Subsequent reactions of $Ca_{12}Li_xZn_{59-x}$ (x = 0, 3.3, 5.0, 8.3, 9.4, and 11.7) were undertaken under the same reaction conditions to examine a possible homogeneity width and to obtain a pure-phase product. According to powder X-ray

DOI: 10.1021/acs.inorgchem.6b00612
Inorg. Chem. 2016, 55, 5041−5050

Table 2. Atomic Coordinates for $Ca_{12}Li_{14.95(3)}Zn_{44.05(3)}$

atom	Wyckoff site	occupancy (%)	x	y	z	U_{eq} (Å^2)
Ca1	18h	1	0.4698(1)	$-x$	0.2896(1)	0.012(1)
Ca2	18h	1	0.8059(1)	$-x$	0.1328(1)	0.013(1)
Zn1	18h	1	0.4350(1)	$-x$	0.1300(1)	0.012(1)
Zn2	18h	1	0.5006(1)	$-x$	0.0868(1)	0.013(1)
Zn3	18h	1	0.5019(1)	$-x$	0.1749(1)	0.012(1)
Li4	18h	1	0.5060(8)	$-x$	0.2299(2)	0.018(3)
Zn/Li5	18h	38.1/61.9(3)	0.5055(1)	$-x$	0.3501(1)	0.017(1)
Zn6	18h	1	0.5049(1)	$-x$	0.4052(1)	0.016(1)
Zn7	18h	1	0.5676(1)	$-x$	0.0436(1)	0.013(1)
Zn8	9e	1	$^1/_2$	0	0	0.013(1)
Zn/Li9	6c	65.4/34.6(6)	0	0	0.0500(1)	0.028(1)
Zn/Li10	6c	42.7/57.3(6)	0	0	0.0952(1)	0.030(1)
Zn11	6c	1	0	0	0.1502(1)	0.019(1)
Zn/Li12	6c	12.2/87.8(5)	0	0	0.2477(1)	0.009(2)
Zn/Li13	6c	75.3/24.7(6)	0	0	0.3309(1)	0.012(1)
Zn14	6c	1	0	0	0.4226(1)	0.011(1)
Li15	3b	1	0	0	$^1/_2$	0.012(6)
Zn/Li16	3a	85.3/14.7(8)	0	0	0	0.027(1)

Table 3. Atomic Coordinates for $Ca_{15}Li_{19.07(2)}Zn_{55.93(2)}$

atom	Wyckoff site	occupancy (%)	x	y	z	U_{eq} (Å^2)
Ca1	12k	1	0.1374(2)	$2x$	0.6461(1)	0.013(1)
Ca2	12k	1	0.5276(2)	$2x$	0.5401(1)	0.013(1)
Ca3	6h	1	0.4691(3)	$2x$	$^1/_4$	0.012(1)
Zn1	12k	1	0.1016(1)	$2x$	0.0436(1)	0.013(1)
Zn2	12k	1	0.1664(1)	$2x$	0.1982(1)	0.014(1)
Zn3	12k	1	0.1673(1)	$2x$	0.0950(1)	0.014(1)
Zn4	12k	1	0.1684(1)	$2x$	0.5098(1)	0.012(1)
Li5	12k	1	0.170(2)	$2x$	0.5745(6)	0.023(5)
Zn/Li6	12k	72.5/27.5(7)	0.1721(2)	$2x$	0.7174(1)	0.015(1)
Zn7	12k	1	0.2345(1)	$2x$	0.1463(1)	0.013(1)
Zn/Li8	12k	96.3/3.7(7)	0.5048(1)	$2x$	0.1122(1)	0.018(1)
Zn/Li9	12k	8.2/91.8(7)	0.5065(8)	$2x$	0.1786(2)	0.016(3)
Zn10	6h	1	0.0990(2)	$2x$	$^1/_4$	0.019(1)
Zn/Li11	4f	15/85(1)	$^1/_3$	$^2/_3$	0.0958(3)	0.010(4)
Zn12	4f	1	$^1/_3$	$^2/_3$	0.1952(1)	0.014(1)
Zn13	4f	1	$^1/_3$	$^2/_3$	0.5185(1)	0.018(1)
Zn/Li14	4f	36/64(1)	$^1/_3$	$^2/_3$	0.5813(2)	0.027(2)
Zn/Li15	4f	93/7(1)	$^1/_3$	$^2/_3$	0.6357(1)	0.032(1)
Zn16	4f	1	$^1/_3$	$^2/_3$	0.6947(1)	0.023(1)
Zn17	4e	1	0	0	0.0922(1)	0.012(1)
Zn/Li18	4e	56/44(1)	0	0	0.7006(1)	0.012(1)
Zn/Li19	2d	46/54(2)	$^1/_3$	$^2/_3$	$^3/_4$	0.025(3)
Li20	2a	1	0	0	0	0.02(1)

diffraction analyses, the desired pure-phase products of $Ca_{12}Li_xZn_{59-x}$ were obtained from the x = 8.3 and 9.4 reactions, giving support to the refined compositions and phase widths (see below). In contrast, all other $x \neq 0$ reactions yielded two-phase mixtures. The x = 11.7 reaction yielded a second new phase that was established as $Ca_{15}Li_{19.07(3)}Zn_{55.93(3)}$ [$P6_3/mmc$, Z = 2, a = 9.183(1) Å, and c = 45.191(5) Å]. So, subsequent reactions of $Ca_{15}Li_xZn_{75-x}$ (x = 15.0, 19.0, 25.0, and 30.0) were designed and carried out under the same heating profiles. However, the products of reactions for x = 15.0, 19.0, and 25.0 contain mixtures of $Ca_{12}Li_xZn_{59-x}$ and $Ca_{15}Li_xZn_{75-x}$ in different ratios, whereas for x = 30.0, a mixture of $Ca_{15}Li_xZn_{75-x}$ and recently found $Ca_{\sim 30}Li_{3+x}Zn_{60-x}$ occurs.[7] Attempts were also made to check whether the same structure types exist in the Li−Ca−Cu system, but neither phase was found, judging from powder X-ray diffraction data.

The phase widths were established using a combination of powder and single-crystal X-ray diffraction analyses. The lattice parameters for $Ca_{12}Li_xZn_{59-x}$ ($R\bar{3}m$) fall in a range of a = 9.074(1)−9.1699(2) Å and c = 53.353(1)−53.602(1) Å, with refined x changing from 5.65(3) to 14.95(3). In contrast, the phase width for $Ca_{15}Li_xZn_{75-x}$ is expected to be much smaller because lattice parameter variations are negligible judging from powder patterns. Figure 1 sketches phase regions of all known ternaries in the Ca−Li−Zn system for a 400 °C section. Without Ca/Li mixings, $Ca_{12}Li_xZn_{59-x}$ ($R\bar{3}m$) and $Ca_{15}Li_xZn_{75-x}$ ($P6_3/mmc$) fall in a narrow band extending from the solid solution of the $CaCu_5$-type $Ca(Li_xZn_{1-x})_5$ ($x \leq$

DOI: 10.1021/acs.inorgchem.6b00612
Inorg. Chem. 2016, 55, 5041−5050

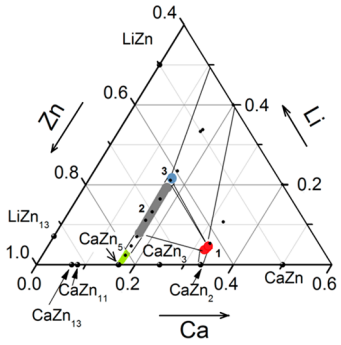

Figure 1. Partial phase triangle of the Li–Ca–Zn system at 400 °C. Phase regions of $Ca_{12}Li_xZn_{59-x}$ (gray) and $Ca_{15}Li_xZn_{75-x}$ (blue) are shaded, together with the recently reported $Ca_{\sim 30}Li_{3+x}Zn_{60-x}$ (red) and the $CaCu_5$-type $Ca(Li_xZn_{5-x})$ solid solution (green).

3.3). However, a phase gap between $Ca_{12}Li_xZn_{59-x}$ ($R\bar{3}m$) and $Ca_{15}Li_xZn_{75-x}$ ($P6_3/mmc$) was not determined because of the difficulty in getting a pure product of the latter phase.

Structure of $Ca_{12}Li_xZn_{59-x}$. Both $Ca_{12}Li_xZn_{59-x}$ ($R\bar{3}m$) and $Ca_{15}Li_xZn_{75-x}$ ($P6_3/mmc$) represent new structure types with Pearson symbols *h*R213 and *h*P180, respectively. For trigonal-phase $Ca_{12}Li_{14.95(3)}Zn_{44.05(3)}$ [$R\bar{3}m$, a = 9.1699(2) Å, c = 53.602(1) Å, and Z = 3], environments of all special Wyckoff sites with 3*m* and −3*m* symmetries are shown in Figure 2. Of these, M11, M10, M9, and M16 atoms form a seven-atom linear chain starting from Zn11, passing through M10, M9, M16, M9, and M10 atoms and ending at another Zn11. The interatomic distances within the chain vary from d_{M9-M10} = 2.424(5) Å, which is the shortest bond in the structure, to d_{M9-M16} = 2.680(3) Å to $d_{M10-Zn11}$ = 2.947(4) Å. However, their −ICOHP values are all reasonably close, from 0.98 to 1.14 eV/bond (see Table 4), indicating that a geometry restriction or matrix effect exists here. This seven-atom chain bridges dimers and trimers of deltahedral clusters centered by M12, M13, Zn14, and Li15 atoms shown in Figure 2b–e.

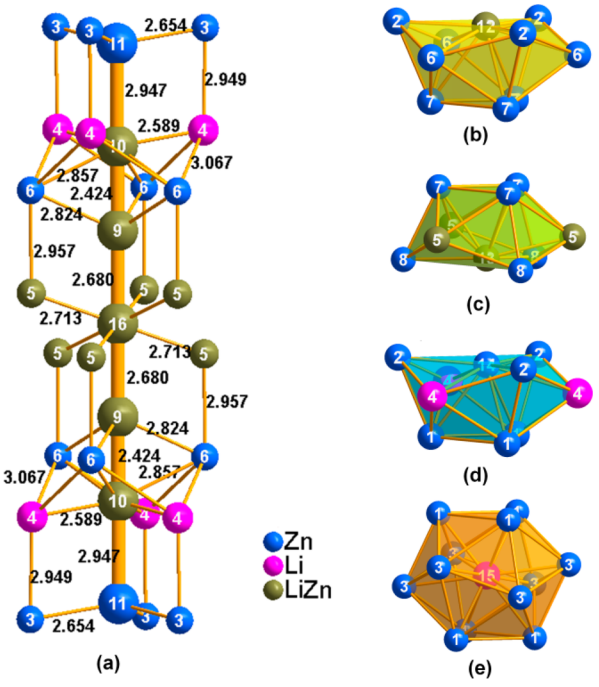

Figure 2. Environments of (a) the seven-atom linear chain and (b) M12, (c) M13, (d) Zn14, and (e) Li15 atoms, all occupying special Wyckoff sites with 3*m* and −3*m* symmetries in the structure of $Ca_{12}Li_{14.95(3)}Zn_{44.05(3)}$. Numbers denote the respective atomic sites, as listed in Table 2. Representative bond distances about the chain are shown.

As shown in Figure 2a, the M16 atom at the Wyckoff 3a site is surrounded by two M9 and six M5 atoms that define a cube slightly squeezed along the *c* axis, as reflected by their respective bond distances, d_{M16-M9} = 2.680 Å versus d_{M16-M5} = 2.713 Å. Each M9 atom is surrounded by three M5 and three Zn6 atoms that define a trigonal prism, together with M16 and M10 capping atoms on the respective M5–M5–M5 and Zn6–Zn6–Zn6 triangular faces. The polyhedron surrounding M10 can also be described as a cube but elongated along *c*. The distortion probably arises from the occupation of three neighboring vertices by Li4, which push Zn11 sites away from the center along *c* ($d_{M10-Zn11}$ = 2.947 Å), because the metallic radius for Li is larger than that for Zn (1.549 vs 1.339 Å).[19] However, the apparent M10–Zn11 bond strength, as evaluated by the ICOHP results, is on the same order as other Zn/Li–Zn/Li bonds with shorter distances (Table 4). The terminating Zn11 atom is somewhat special because it adopts a tetrahedral environment defined by one M10 and three Zn3 atoms.

Regarding the deltahedral clusters in this structure, Li15 is located at the center of an icosahedron, i.e., Li15@$(Zn1)_6(Zn3)_6$ (orange). On the other hand, the M12, M13, and Zn14 sites occupy the centers of *hypho*-icosahedra, viz., M12@$(Zn2)_3(Zn6)_3(Zn7)_3$ (yellow), M13@$(M5)_3(Zn7)_3(Zn8)_3$ (lime), and Zn14@$(Zn1)_3(Zn2)_3(Li4)_3$ (blue). The surface Zn/Li–Zn/Li distances within all of these three-atom defect icosahedra are comparable to the center–vertex distances (cf. Table 4), probably because of electron delocalization. The corresponding Li4 site of M10- and Zn14-centered polyhedral clusters is occupied by a Zn/Li mixture in $Ca_{12}Li_xZn_{59-x}$ with lower x; e.g., it is refined as 66.0/34.0(3)% Zn/Li for x = 5.65(3) and 22.0/78.0(4)% for x = 9.44(3).

With the foregoing basic clusters in mind, now we consider the cluster linkages. Neighboring M12- and M13-centered *hypho*-icosahedra share a Zn7–Zn7–Zn7 triangular face to form a dimer (D; Figure 3a). Similarly, each Li15-centered icosahedron and two M14-centered *hypho*-icosahedra form a trimer (T) by sharing Zn1–Zn1–Zn1 triangular faces (Figure 3b). Each dimer shares all of its Zn8 vertices with neighboring dimers and all Zn2 vertices with trimers. In addition, each M5 site is exobonded to M16 atoms, and each Zn6 position is exobonded to M9 and M10 atoms of the linear chain. However, Zn7 atoms on the waist of the dimer do not connect with other clusters or the chain. Overall, each dimer has nine exobonds, all to the seven-atom bridging chain. As for the trimer, all six Zn2 atoms are shared with neighboring dimers, whereas the six Zn3 and six Li4 atoms are each exobonded to M10 and Zn11 atoms of the seven-atom chains, respectively. Thus, each trimer has 12 exobonds to the seven-atom bridging chains.

Figure 4 shows the (010) projection of the structure of $Ca_{12}Li_{14.95(3)}Zn_{44.05(3)}$, represented by dimers (D), trimers (T), and chains, together with a (001) projection of three representative slabs at different heights along the *c* axis. The structural motif features an extended framework of corner-shared dimers and trimers that are reinforced by seven-atom bridging chains. Each unit cell is composed of six dimers, three trimers, and three chains. From another viewpoint, the

DOI: 10.1021/acs.inorgchem.6b00612
Inorg. Chem. 2016, 55, 5041–5050

Table 4. Selected Bond Distances (Å) for $Ca_{12}Li_{14.95(3)}Zn_{44.05(3)}$ and Corresponding −ICOHP Values (eV/bond)

bond	distance	−ICOHP	bond	distance	−ICOHP	bond	distance	−ICOHP
Chain-to-Cluster and In-Chain Bonds								
Zn11−Zn3	2.654(1)	1.77	M9−Zn6	2.824(1)	0.35	M9−M16	2.680(3)	1.14
M10−Li4	2.59(1)	1.61	M16−M5	2.713(2)	1.35	M10−Zn11	2.947(4)	0.98
M10−Zn6	2.857(2)	0.98	M9−M10	2.424(5)	1.02			
Center-to-Vertex Bonds								
M12−Zn2	2.639(1)	1.22	M13−Zn7	2.711(2)	0.80	Zn14−Li4	2.85(1)	0.86
M12−Zn6	2.823(2)	0.76	M13−Zn8	2.650(1)	1.28	Li15−Zn1	2.542(1)	0.30
M12−Zn7	2.748(6)	0.71	Zn14−Zn1	2.716(2)	0.76	Li15−Zn3	2.713(1)	0.33
M13−M5	2.839(2)	0.76	Zn14−Zn2	2.660(1)	1.29			
Vertex-to-Vertex Bonds								
Zn1−Zn3	2.786(1)	0.98	Zn2−Zn6	2.799(1)	0.99	Zn6−Zn7	2.812(1)	0.81
Zn1−Zn1	2.796(2)	0.94	Zn3−Li4	2.95(1)	0.83	Zn7−Zn7	2.726(1)	0.95
Zn1−Zn2	2.540(1)	1.58	Zn2−Zn7	2.548(1)	1.52	Zn7−Zn8	2.573(1)	1.48
Zn1−Zn3	2.631(1)	1.48	Zn3−Zn3	2.820(1)	1.00	M5−Zn6	2.957(2)	0.91
Zn1−Li4	2.78 (1)	0.98	M5−Zn7	2.780(2)	0.85			
Zn2−Li4	2.843(7)	0.92	M5−Zn8	2.837(1)	0.96			

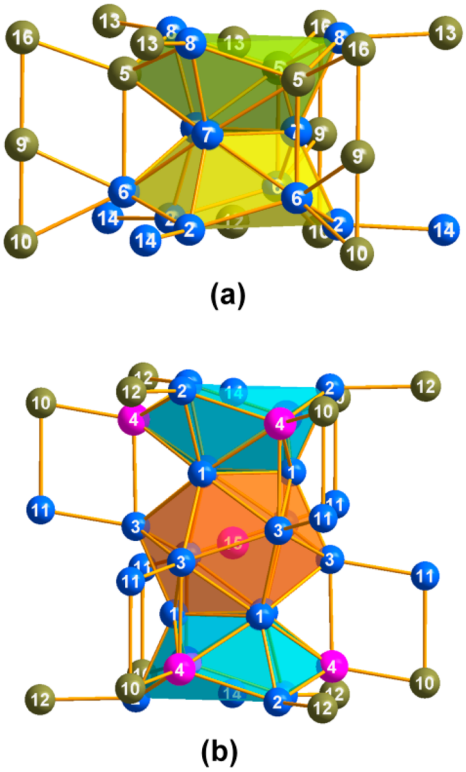

Figure 3. Building units of (a) a dimer and (b) a trimer of deltahedral clusters and fragments and their linkages in the structure of $Ca_{12}Li_{14.95(3)}Zn_{44.05(3)}$.

structure can be viewed as a packing of dimer and trimer slabs along the *c* axis, with a sequence of DTDDTDDTD.

The locations of the formal countercations can be seen from the three representative slabs in Figure 4b−d. As a result of 3-fold rotational symmetry, both Ca1 and Ca2 sites self-aggregate into $(Ca1)_3$ and $(Ca2)_3$ triangular units. These are respectively located at the same heights as the shared triangular faces of dimers or trimers (above). Each $(Ca1)_3$ is enclosed by three in-plane dimers (Figure 4b,c), together with one dimer and one trimer respectively capping the top and bottom (Figure 4a). In comparison, the $(Ca2)_3$ triangles in the trimer slabs are interlinked through shorter vertical Ca−Ca bonds [3.738 Å; see Figure 4a,d].

Figure 5 shows the Li/Zn ratios at specific sites as a function of the refined composition of $Ca_{12}Li_xZn_{59-x}$, $x \approx 5.65(3)$−14.95(3). A total of 9 out of 16 sites involve Li/Zn variations over the whole composition range. Of these sites, M15 and M6 show inverse proportions, and the remaining seven sites show a positive response to increasing Li content. Notably, the M10, M12, and M13 sites are free of Li at the lower phase boundary $x = 5.65(3)$. In contrast, Li occupancy at the M6 site decreases until it is completely depleted at the upper phase boundary $x = 14.95(3)$. In general, all of these changes occur around either polyhedral centers or bridging atoms.

Structure of $Ca_{15}Li_xZn_{75-x}$. $Ca_{15}Li_xZn_{75-x}$ ($P6_3/mmc$) exhibits common structural motifs (Figure 6) with those of $Ca_{12}Li_xZn_{59-x}$ ($R\bar{3}m$), in particular, dimers, trimers, and linear bridging chains, but some of these features are different. First, $Ca_{15}Li_xZn_{75-x}$ contains an additional type of dimer slab (pale blue, located at $z = {}^1/_4$ and ${}^3/_4$; see Figure 6a). The new dimer is generated from M18-centered *hypho*-icosahedra only (Figure 6f). As a result of this additional slab, the bridging chain is a nine-atom chain, as defined by Zn13−M14−M15−Zn16−M19−Zn16−M15−M14−Zn13. Meanwhile, there is another set of triangular units $(Ca3)_3$ located around this new slab. Therefore, each unit cell of $Ca_{15}Li_xZn_{75-x}$ ($P6_3/mmc$) contains six dimers (D), two trimers (T) and two nine-atom linear chains. Also, the stacking sequence of dimers and trimers along *c* is TDDDTDDD, in contrast to DTDDTDDTD for the trigonal-phase $Ca_{12}Li_xZn_{59-x}$ ($R\bar{3}m$).

Family of Intergrowth Structures. As shown above, if atomic decorations and negligible differences in the geometry in both foregoing structures are not considered, all dimers contain two atoms located at polyhedral centers, three atoms at the waist, six vertex atoms exobonded to linear chains, and another six vertex atoms shared with neighboring dimers or trimers. A dimer of *hypho*-icosahedra can be denoted as M_{14} (M = Zn/Li) = $[M@M_{3/2}M_3M_{3/2}]_2$. Similarly, each trimer can be written as $M_{24} = [M@M_6M_{6/2}](M@M_{3/2}M_6)_2$ containing three atoms at polyhedral centers, six atoms on the waist without exobonding, 12 atoms with exobonding, and six atoms shared with neighboring dimers. Also, the heights of the dimer and trimer (4.8 and 8.2 Å) barely change with variation of the chemical composition.

DOI: 10.1021/acs.inorgchem.6b00612
Inorg. Chem. 2016, 55, 5041−5050

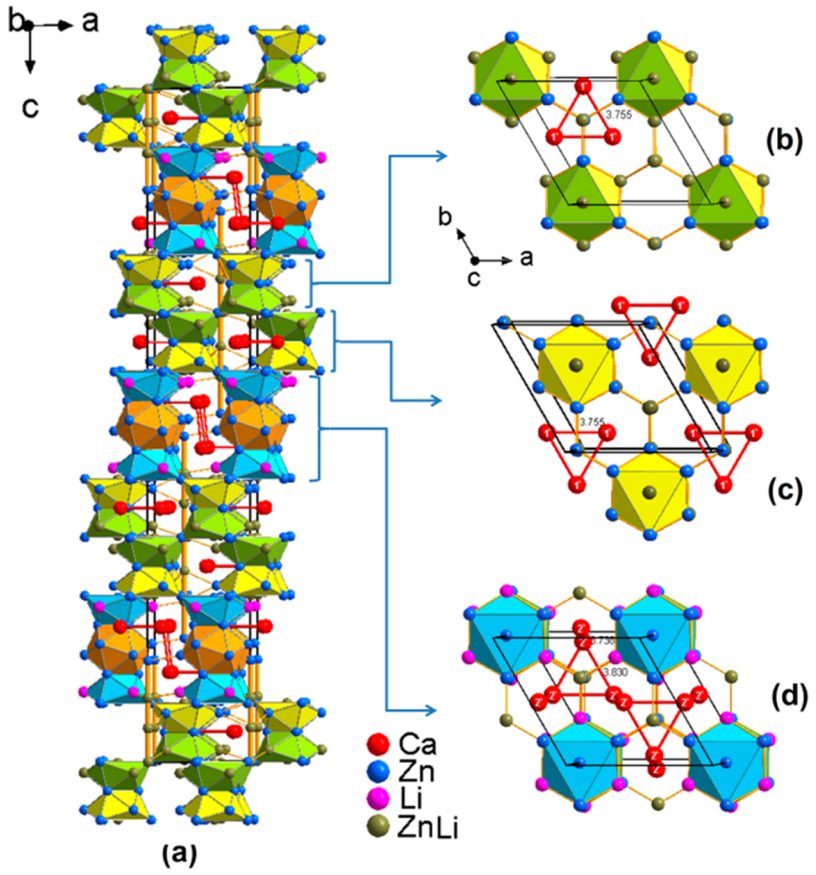

Figure 4. (a) Polyhedral representation of the structure of $Ca_{12}Li_{14.95(3)}Zn_{44.05(3)}$ in the (010) direction. (b–d) Slabs of dimers and trimers projected along the (001) direction.

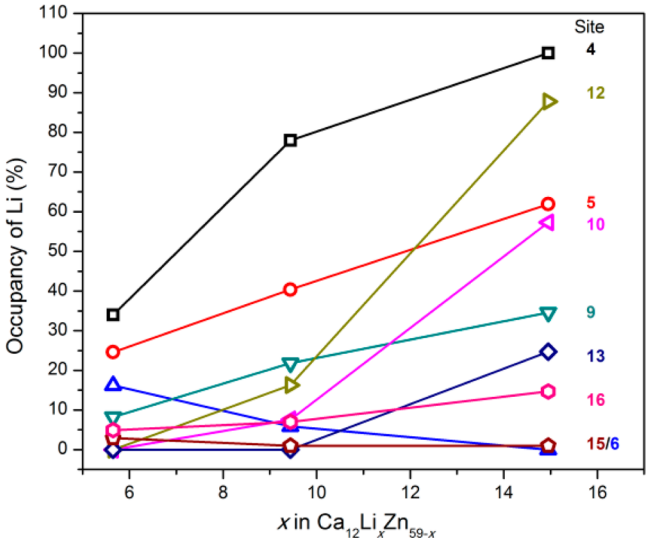

Figure 5. Occupancy variations of Li at different sites for Zn/Li mixtures in $Ca_{12}Li_xZn_{59-x}$ [x = 5.65(3), 9.44(3), and 14.95(3)].

Therefore, both the trigonal-phase $Ca_{12}Li_xZn_{59-x}$ and hexagonal-phase $Ca_{15}Li_xZn_{75-x}$ structures can be considered as intergrowth structures of M_{14} and M_{24} slabs. The intergrowth family can be described by a general formula of $(A_{3m+6n})(L_{2m+3n})(M_{14})_m(M_{24})_n$, in which A and L denote countercations and linear chain atoms, respectively. The member $A_{36}L_{21}M_{156}$ with m = 6 and n = 3 corresponds to the structure of $Ca_{12}Li_xZn_{59-x}$ (Z = 3), whereas $A_{30}L_{18}M_{132}$ with m = 6 and n = 2 corresponds to $Ca_{15}Li_xZn_{75-x}$ (Z = 2).

A survey of the literature reveals that several other valence-electron-poor examples can be grouped into this intergrowth family. As listed in Table 5, the $EuMg_{5.2}$-type structure (e.g., $SrMg_{5.2}$)[20] represents one of the basic types with m = 2 and n = 0, and $Ba_2Li_{4.21}Al_{4.79}$[21] represents the other basic type with m = 0 and n = 3. In comparison, $Sr_9Li_{17.5}Al_{25.5}$[21] (m = 2 and n = 2) consists of two dimers and two trimers, with a repeating sequence of DTDT. The structures of these three compounds are shown in Figure 7a–c. Besides these known examples, other compositions can also be extrapolated according to the general formula, together with the corresponding lattice parameter c (=4.8m + 8.2n). For example, "$Ca_9L_5M_{38}$" (m = 1 and n = 1; c = 13.2 Å), "$Ca_{12}L_5M_{54}$" (m = 2 and n = 1; c = 17.8 Å), "$Ca_{15}L_8M_{62}$" (m = 1 and n = 2; c = 21.2 Å), and "$Ca_{15}L_9M_{66}$" (m = 3 and n = 1; c = 22.6 Å) can be easily derived for the Ca–Li–Zn system. What could be challenging is the synthesis of these unknown phases because the (L + M)/Ca ratios fall in a small range, ~5.0 ± 0.3. Moreover, some of them might exhibit modified structural motifs (below) and/or might be thermodynamically unstable.

In the literature, some other structures containing modified defect deltahedral clusters are closely related to this intergrowth family. For example, the structure of Sr_9Mg_{38},[22] which was earlier described as $SrMg_4$,[23] may be considered as a packing of similar dimer slabs, with half being "defect" dimers (Figure 7d). The structure of $BaLi_4$[23] (Figure 7e) might be considered as another basic type (m = 0 and n = 1) of this intergrowth family; however, the centers of yellow-shaded *hypho*-icosahedra in

DOI: 10.1021/acs.inorgchem.6b00612
Inorg. Chem. 2016, 55, 5041–5050

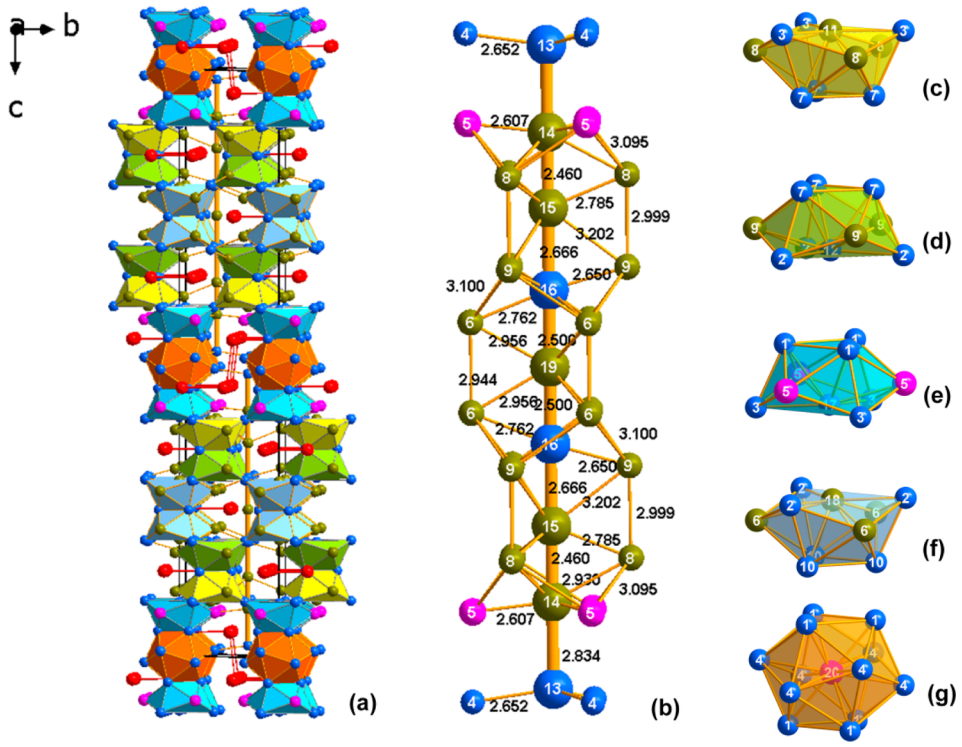

Figure 6. (a) Polyhedral view of the structure of $Ca_{15}Li_{19.07(2)}Zn_{55.93(2)}$ ($P6_3/mmc$) projected in the (100) direction, together with details of (b) the nine-atom linear chain and colored *hypho*-icosahedral and icosahedral clusters shown in parts c–g in transparent mode.

Table 5. List of Some Derived Intergrowth Structures of the $(A_{3m+6n})(L_{2m+3n})(M_{14})_m(M_{24})_n$ Family, Known Examples, and Corresponding VEC and *e*/*a* Values

formula	*m*, *n*	example	VEC	*e*/*a*	ref
$A_6L_4M_{28}$	2, 0	$SrMg_{5.2}$ (Z = 6)	2.38	2.00	20
$A_{18}L_9M_{72}$	0, 3	$Ba_2Li_{4.21}Al_{4.79}$ (Z = 9)	2.51	2.05	21
$A_{18}L_{10}M_{76}$	2, 2	$Sr_9Li_{17.5}Al_{25.5}$ (Z = 2)	2.60	2.15	21
$A_{36}L_{21}M_{156}$	6, 3	$Ca_{12}Li_{15}Zn_{44}$ (Z = 3)	2.15	1.79	this work
$A_{30}L_{18}M_{132}$	6, 2	$Ca_{15}Li_{19}Zn_{56}$ (Z = 2)	2.15	1.79	this work

$BaLi_4$ move slightly toward the gray-shaded icosahedra, resulting in a shortening of the *c* lattice parameter.

Structural Realization via the Zintl–Klemm Concept. Because both structures can be described as built of deltahedral clusters, can these two structures be rationalized by the Zintl–Klemm concept taking into account Wade–Mingos[24,25] or Jemmis rules[26] for cluster bonding? The same endeavor works fairly well for the structure of $Ca_{\sim 30}Li_{3+x}Zn_{60-x}$ (x = 0.44–1.38), which contains an extended network of Zn_3 triangles, Zn_{12} icosahedra, and $(Li,Zn)_{18}$ tubular clusters.[7] To evaluate VEC required for bonding, extended Hückel molecular orbital (EHMO) calculations[27] on isolated $Zn_2@Zn_{15}^{22-}$ and $LiZn_2@Zn_{24}^{31-}$ clusters terminated with H-like atoms with an orbital energy of the Zn 4p atomic orbitals have been carried out (Figure S1 in the Supporting Information). Large negative charges are necessary to optimize bonds for the isolated dimer and trimer because Zn has only two valence electrons. The EHMO calculations yielded optimized VEC values of $56e^-$ and $84e^-$ for a dimer and a trimer, at which a turnover from bonding to antibonding character is observed. In fact, both VEC values do not change regardless of whether the cluster centers are occupied or not and no matter whether Zn or triels (e.g., Ga) occupy vertices. For bridging atoms in linear chains, a formal charge can be simply calculated following the 18 − *N* rule. For example, each 4-bonded Zn11 in $Ca_{12}Li_xZn_{59-x}$ requires two electrons to fulfill its valence shell, thus a negative formal charge of 2−. In contrast, each 8-bonded Zn9, Zn10, and Zn16 may be regarded as a cation with a formal charge of 2+. According to the Zintl–Klemm concepts[28–32] or Jemmis *mno* rules,[26] it is easier to figure out that each shared corner for a condensed cluster will reduce VEC by one electron. For example, corner-sharing double icosahedra will have a total of 52 skeleton and 23 exobond electrons. In other words, for condensed clusters, the number of skeletal electrons still follows the 2*n* + 2 rule, but the number of exobonds decreases for each shared corner. In the present cases, all shared corners are double-counted, so the final VEC must subtract the number of shared corners.

Table 6 summarizes tentative electron-counting schemes for both the trigonal-phase $Ca_{12}Li_xZn_{59-x}$ and primitive hexagonal-phase $Ca_{15}Li_xZn_{75-x}$. As seen in Table 6, there is a shortage of $40e^-$/formula unit for $Ca_{12}Li_xZn_{59-x}$ following the Zintl–Klemm concept. With the Li percentage increasing in $Ca_{12}Li_xZn_{59-x}$, a larger number of deficient electrons are observed. Such a large discrepancy makes it hard to classify the title compounds as Zintl phases. In fact, some vertex atoms of dimers and trimers show more complex bonding interactions than are usually seen for deltahedral clusters. For example, each Zn6 vertex of the dimer in $Ca_{12}Li_xZn_{59-x}$ has two exobonds together with M5–M6 interpolyhedra bonds (Figure 3a). M4–M3 interpolyhedra bonds also exist for the trimers (Figure 3b). Complex bonding interactions imply higher coordination numbers, an outcome that is typical for close-packed metals and Hume-Rothery phases with low VEC. Previously, Haüssermann and co-workers[21] have nicely described the structures of $Ba_2Li_{4.21}Al_{4.79}$ and $Sr_9Li_{17.5}Al_{25.5}$, members of the same intergrowth family, as hexagonally close-packed tetrahe-

DOI: 10.1021/acs.inorgchem.6b00612
Inorg. Chem. 2016, 55, 5041–5050

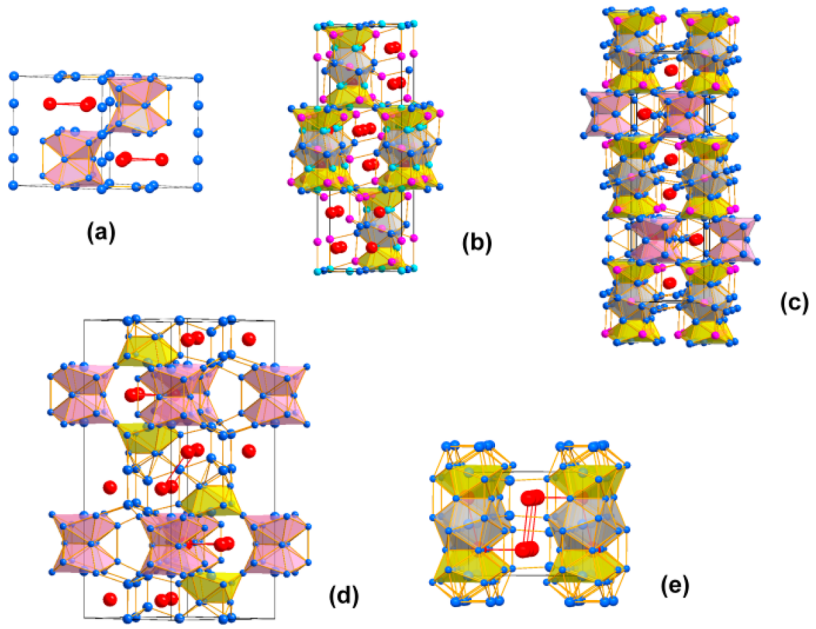

Figure 7. Crystal structures of (a) $SrMg_{5.2}$, (b) $Ba_2Li_{4.21}Al_{4.79}$, (c) $Sr_9Li_{17.5}Al_{25.5}$, (d) Sr_9Mg_{38}, and (e) $BaLi_4$ with dimers (pink) and trimers (yellow-gray) shown in polyhedra. In general, red spheres represent positive cations (Sr and Ba), and blue, pink, and cyan spheres represent electronegative atoms (Mg, Li, and Al).

Table 6. Tentative Electron-Counting Scheme for $Ca_{12}Li_xZn_{59-x}$ and $Ca_{15}Li_xZn_{75-x}$

	$Ca_{12}Li_xZn_{59-x}$	$Ca_{15}Li_xZn_{75-x}$
VEC of the dimer/cell	56 × 6 = 336	56 × 6 = 336
VEC of the trimer/cell	84 × 3 = 252	84 × 2 = 168
no. shared corners/cell	54	48
charge of the linear chain/cell	3 × 6+ = 18+	2 × 10+ = 20+
no. of electrons required/cell	336 + 252 − 54 − 18 = 516	336 + 168 − 48 − 20 = 436
no. of electrons provided by the components/cell	395 ± 15	324
difference/formula units	40 ± 5	56

dral stars and double tetrahedral stars. In fact, the values of VEC per electronegative atom for $Ca_{12}Li_xZn_{59-x}$ (2.15−2.32) and $Ca_{15}Li_xZn_{75-x}$ (~2.16) are electronically positioned near the Hume-Rothery phases and sp-bonded close-packed metals (≤2). In contrast, the Zintl-like phase $Ca_{\sim 30}Li_{3+x}Zn_{60-x}$ (2.90) is much higher, close to the region of polar intermetallic and Zintl phases (>3.5). If the average VEC per atom (e/a) rather than VEC (per electronegative atom) is used as an indicator, the e/a values for both phases are 1.79 (cf. Table 5), close to those of typical Hume-Rothery phases, e.g., 1.57−1.68 for γ-$Cu_{5-x}Zn_{8+x}$,[6,33] 1.61−1.66 for rhombohedrally distorted γ-$Au_{5-x}Zn_{8+y}$,[34] and 1.7−2.2 for quasicrystals and approximants.[35] In the following, we will continue to check whether a Hume-Rothery mechanism applies for the present phases through first-principles electronic structure calculations.

Hume-Rothery Stabilization Mechanism. As shown in Figure 8, the electronic density of states (DOS) curve of hypothetical "$Ca_{12}LiZn_{58}$" is typical of a polar intermetallic compound, with Fermi energy (E_F) located in a minimum (pseudogap) of a continuous DOS. On both sides of E_F, the DOS is dominated by Zn 4s4p and Ca 3d states, although the Ca 3d states have greater contributions at higher energies, i.e., +2.0−6.0 eV. Similar features appear for the primitive hexagonal structure "$Ca_{15}Li_{18}Zn_{57}$" (Figure S2 in the

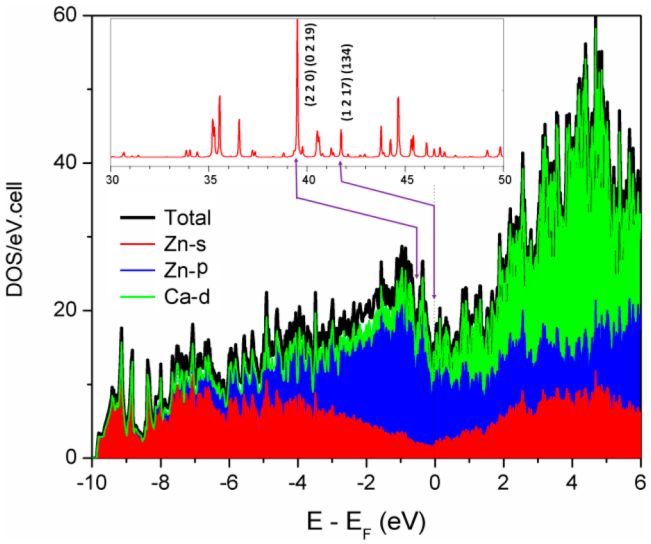

Figure 8. DOSs for hypothetical "$Ca_{12}LiZn_{58}$", a model modified from the structure of $Ca_{12}Li_{14.95(3)}Zn_{44.05(3)}$ by assuming that Li/Zn mixed sites on cluster vertices of $Ca_{12}Li_{14.95(3)}Zn_{44.05(3)}$ are occupied by Zn only. The relationship between the X-ray diffraction peaks and pseudogaps around the Fermi energy is also shown.

Supporting Information). Adding Li atoms to the structure increases the contribution of Li 2s states in the energy range of −9.0 to −2.0 eV, as seen for the hypothetical "$Ca_{12}Li_{15}Zn_{44}$" (cf. Figure S2 in the Supporting Information). These features confirm metallic character for the present phases, similar to that of Zn metal.

The Hume-Rothery stabilization mechanism involves identification of the sets of Miller planes (hkl) that form a polyhedron, called a Jones zone, in reciprocal space with distances from a reciprocal lattice point that very nearly match the radius of the Fermi sphere. Via the periodic potential, the electronic states associated with these Fermi wave vectors can

DOI: 10.1021/acs.inorgchem.6b00612
Inorg. Chem. 2016, 55, 5041−5050

mix, resulting in energy gaps in these regions of the band structure and the formation of a pseudogap in the resulting DOS curve at E_F for such Hume-Rothery phases. Mizutani denoted these Miller planes as critical lattice planes.[33] For γ-brass-type structures, the formation of a pseudogap is related to critical lattice planes (330) and (411), whereas for Mackay-, Bergman- and Tsai-type quasicrystal approximants, the (543), (710), and (550) Miller planes are critical.[33] In hexagonal-phase "$Ca_{12}LiZn_{58}$", the diameter of the Fermi sphere is 1.451 $Å^{-1}$ according to TB-LMTO calculations. This value matches the interplane value (1.447 $Å^{-1}$) of the zone defined by (1,2,17) and (134) planes (inset of Figure 8). These planes correspond to the strong peak in the powder X-ray diffraction pattern located at $2\theta \sim 41.7°$ and with an intensityI/I_{max} of ca. 18%. Meanwhile, the pseudogap at ∼−0.5 eV corresponds to the strongest diffraction peak at ∼39.5°. Similarly, the Fermi sphere of the primitive hexagonal structure "$Ca_{15}Li_{18}Zn_{57}$" inscribes the Jones zone defined by the (2,0,16), (220), and (3,0,10) planes, which correspond to the strongest peak at $2\theta \sim 39.2°$ in the powder pattern (Figure S2 in the Supporting Information). The band structure also shows a real gap at E_F along the (001) direction for both structures (Figure S3 in the Supporting Information). Judging from the foregoing results, we may conclude that the stability of both Ca−Li−Zn phases utilizes the Fermi surface−Brillouin zone interaction mechanism adopted by the Hume-Rothery phases.[5,6,33]

CONCLUSION

The discovery of $Ca_{12}Li_xZn_{59-x}$ and $Ca_{15}Li_xZn_{75-x}$ proves that lithiation of Ca−Zn binary phases continues to yield fruitful results. Both compounds adopt new structure types, consisting of rarely seen building blocks of dimers of face-sharing *hypho*-icosahedra and trimers of two *hypho*-icosahedra sandwiching an icosahedron. With these building units in mind, a large family of intergrowth structures can be formulated, $(A_{3m+6n})(L_{2m+3n})(M_{14})_m(M_{24})_n$, which also include several known structural types. In contrast to the more Zintl-like $Ca_{\sim 30}Li_{3+x}Zn_{60-x}$, these two compounds are closer to sp-bonded metals in light of their valence electron numbers. In fact, their structural stabilities can be rationalized by a Fermi surface−Brillouin zone interaction mechanism, which is adopted by the Hume-Rothery phases. The present study and recent work[7] on lithiation of $CaZn_2$ demonstrate that a paradigm shift from Zintl-like intermetallics to Hume-Rothery phases can be accomplished through lithiation of binary intermetallics.

Apparently, profound cluster chemistry exists for polar intermetallics with VECs between 2.0 and 3.0. Compounds with VECs falling in this region are akin to the electron-richer Zintl phases on one side and electron-poorer Hume-Rothery phases on the other side. For the Ca−Li−Zn system, structural versatility originates from not only the viable Li/Zn mixings but also the molar ratio of Ca:(Li + Zn). In terms of Zn-cluster formation, isolated or linked Zn_{12} icosahedra would be rare because of the large discrepancy between VECs required for cluster stabilization (26 skeletal plus 12 exobonded electrons) and the valence electrons contributed by Zn ($12 \times 2 = 24$). In contrast, the difference for an icosahedral cluster defined by group 13 elements is much smaller ($38 - 12 \times 3 = 2$). This study illustrates how a structure responds to a limited available VEC, that is, to form condensed deltahedra via sharing corners, edges, and faces or condensed and defect deltahedra (*nido*, *arachno*, and *hypho*) that require even fewer skeletal electrons. The existence of condensed and defect deltahedra in the present structures reminds one of their structural kinship to Zintl phases dominated by neighboring group 13 elements (Ga, In, and Tl).

ASSOCIATED CONTENT

Supporting Information

The Supporting Information is available free of charge on the ACS Publications website at DOI: 10.1021/acs.inorgchem.6b00612.

Molecular orbital of isolated $Zn_2@Zn_{15}^{22-}$ and $LiZn_2@Zn_{24}^{31-}$ clusters (Figure S1), DOSs of hypothetical "$Ca_{12}Li_{15}Zn_{44}$" and "$Ca_{15}Li_{18}Zn_{57}$" models (Figure S2), and band structures of "$Ca_{12}LiZn_{58}$" and "$Ca_{15}Li_{18}Zn_{57}$" models (Figure S3) (PDF)

CIF file (CIF)

AUTHOR INFORMATION

Corresponding Author

*E-mail: qslin@ameslab.gov (Q.L.).

Notes

The authors declare no competing financial interest.

ACKNOWLEDGMENTS

The research was supported by the U.S. Department of Energy (DOE), Office of Basic Energy Sciences, Materials Sciences and Engineering Division. Ames Laboratory is operated for the U.S. DOE by Iowa State University under Contract DE-AC02-07CH11358. R.Z. was an undergraduate student participant of the Department of Chemistry, Iowa State University.

REFERENCES

(1) Wang, F.; Miller, G. J. *Inorg. Chem.* **2011**, *50*, 7625−7636.
(2) Nesper, R. *Z. Anorg. Allg. Chem.* **2014**, *640*, 2639−2648.
(3) Brandon, J. K.; Brizard, R. Y.; Chieh, P. C.; McMillan, R. K.; Pearson, W. B. *Acta Crystallogr., Sect. B: Struct. Crystallogr. Cryst. Chem.* **1974**, *30*, 1412−1417.
(4) Mizutani, U. In *The Science of Complex Alloy Phases*; Massalski, T. B., Turchi, P. E. A., Eds.; The Minerals, Metals & Materials Society: Warrendale, PA, 2005; pp 1−42.
(5) Hume-Rothery, W. *J. Inst. Met.* **1926**, *35*, 295.
(6) Hume-Rothery, W.; Raynor, G. V. *The Structure of Metals and Alloys*, 4th ed.; Institute of Metals: London, 1962.
(7) Lin, Q. *Inorg. Chem.* **2015**, *54*, 922−929.
(8) Fornasini, M. L.; Merlo, F. *Acta Crystallogr., Sect. B: Struct. Crystallogr. Cryst. Chem.* **1980**, *36*, 1739−1744.
(9) Wieting, J. *Naturwissenschaften* **1961**, *48*, 401.
(10) Haucke, W. *Z. Anorg. Allg. Chem.* **1940**, *244*, 17−22.
(11) Wendorff, M.; Roehr, C. *Z. Naturforsch., B: J. Chem. Sci.* **2007**, *62*, 1549−1562.
(12) Wendorff, M.; Röhr, C. *J. Alloys Compd.* **2006**, *421*, 24−34.
(13) *SAINT+*, version 8.30; Bruker AXS Inc.: Madison, WI, 2013.
(14) *SHELXTL*, 6.10 ed.; Bruker Analytical X-ray Systems, Inc.: Madison, WI, 2000.
(15) Tank, R.; Jepsen, O.; Burkhardt, A.; Andersen, O. K. *TB-LMTO-ASA Program*, version 4.7; Max-Planck-Institut für Festkörperforschung: Stuttgart, Germany, 1994.
(16) Shriver, H. L. *The LMTO Method*; Springer-Verlag: Berlin, Germany, 1984.
(17) Andersen, O. K.; Jepsen, O. *Phys. Rev. Lett.* **1984**, *53*, 2571−2574.
(18) Dronskowski, R.; Bloechl, P. E. *J. Phys. Chem.* **1993**, *97*, 8617−8624.
(19) Pauling, L. *The Nature of the Chemical Bond*, 3rd ed.; Cornell University Press: Ithaca, NY, 1960; p 644.

DOI: 10.1021/acs.inorgchem.6b00612
Inorg. Chem. 2016, 55, 5041−5050

(20) Erassme, J.; Brauers, T.; Lueken, H. *J. Less-Common Met.* **1988**, *137*, 155−161.
(21) Häussermann, U.; Wörle, M.; Nesper, R. *J. Am. Chem. Soc.* **1996**, *118*, 11789−11797.
(22) Merlo, F.; Fornasini, M. L. *Acta Crystallogr., Sect. B: Struct. Crystallogr. Cryst. Chem.* **1982**, *38*, 1797−1798.
(23) Wang, F. E.; Kanda, F. A.; Miskell, C. F.; King, A. *Acta Crystallogr.* **1965**, *18*, 24−31.
(24) Wade, K. *Adv. Inorg. Chem. Radiochem.* **1976**, *18*, 1−66.
(25) Mingos, D. M. P. *J. Chem. Soc., Chem. Commun.* **1983**, 706−708.
(26) Jemmis, E. D.; Balakrishnarajan, M. M.; Pancharatna, P. D. *J. Am. Chem. Soc.* **2001**, *123*, 4313−23.
(27) Ren, J.; Liang, W.; Whangbo, M.-H. *CAESAR for Windows*; Prime-Color Software, Inc., North Carolina State University: Raleigh, NC, 1998.
(28) Zintl, E.; Schneider, A. *Z. Elektrochem. Angew. Phys. Chem.* **1935**, *41*, 764−767.
(29) Zintl, E.; Dullenkopf, W. *Z. Physik. Chem.* **1932**, *B16*, 183−194.
(30) Zintl, E. *Angew. Chem.* **1939**, *52*, 1−6.
(31) Schäfer, H. *Annu. Rev. Mater. Sci.* **1985**, *15*, 1−42.
(32) Schäfer, H.; Eisenmann, B.; Müller, W. *Angew. Chem., Int. Ed. Engl.* **1973**, *12*, 694−712.
(33) Mizutani, U. *Hume-Rothery Rules for Structurally Complex Alloy Phases*; CRC Press: London, 2011.
(34) Thimmaiah, S.; Miller, G. J. *Inorg. Chem.* **2013**, *52*, 1328−1337.
(35) Lin, Q.; Corbett, J. D. *Struct. Bonding (Berlin, Ger.)* **2009**, *133*, 1−39.

DOI: 10.1021/acs.inorgchem.6b00612
Inorg. Chem. 2016, 55, 5041−5050